



Study on Properties and Microstructure of Wire Arc Additive Manufactured 2209 Duplex Stainless Steel

Bellamkonda Prasanna Nagasai¹ · Maheshwar Dwivedy¹ · Sudersanan Malarvizhi² · Visvalingam Balasubramanian² · Addanki Ramaswamy³ · Pulivarthi Snehalatha⁴ · Nagavalli Vegesna⁵

Received: 20 January 2024 / Revised: 7 May 2024 / Accepted: 30 May 2024 / Published online: 10 June 2024
© ASM International 2024

Abstract

In the last two decades, wire arc additive manufacturing (WAAM) has emerged as a cost-effective alternative to traditional additive manufacturing (AM) processes, particularly for producing medium-to-large-scale components. The primary advantages of wire-based AM include simplified automated production and enhanced control and flexibility in the fabrication process. In this study, the gas metal arc welding (GMAW) process was used to produce cylindrical components from 2209 duplex stainless steel (DSS) using the WAAM technique. The mechanical properties and microstructural characteristics of the 2209 DSS cylinders were examined. The microstructure of the components varied from the bottom (region (1)) to the top (region (2)), resulting in a hardness difference between 301 HV0.5 and 327 HV0.5, and an impact toughness variation from 118 to 154 J. Additionally, the tensile properties exhibited anisotropic characteristics: the ultimate tensile strength and yield strength ranged from 750 to 790 MPa and from 566 to 594 MPa, respectively. The complex heat cycles and cooling rates during the WAAM process significantly affected the primary phase balance (50/50 austenite/ferrite) in the produced cylinder. In the GMAW-processed component, σ -phase precipitation was observed at the boundaries of the ferrite grains. The increase in the percentage of austenite from region (1) to region (2) was attributed to a decrease in the cooling rate and a longer time for solid-state phase transformation.

Keywords Wire arc additive manufacturing · 2209 duplex stainless steel · Mechanical properties · Microstructural characteristics

Introduction

Manufacturing techniques have evolved significantly over the centuries, transitioning from manual processes to highly automated operations. Traditional manufacturing methods like casting, forging, and machining, have long been industrial cornerstones due to their reliability and established technologies [1]. However, these methods come with inherent disadvantages. Casting may introduce defects such as porosity and unwanted inclusions, limiting its application in high-performance areas. Forging, though it enhances material strength through grain deformation, is constrained by the complexity of shapes it can produce and often involves high operational costs. Machining, while precise, usually results in significant material wastage and prolonged production times, especially for complex parts, limiting flexibility and efficiency in modern manufacturing contexts [2]. Additive manufacturing (AM) represents a paradigm shift in production technology, assembling components layer by layer using

✉ Bellamkonda Prasanna Nagasai
nagasaibellamkonda143@gmail.com

¹ Department of Mechanical Engineering, SRM University-AP, Neerukonda, Mangalagiri Mandal, Guntur, Andhra Pradesh 522240, India

² Department of Manufacturing Engineering, Annamalai University, Annamalai Nagar, Chidambaram 608002, India

³ Department of Mechanical Engineering, SASI Institute of Technology and Engineering, Tadepalligudem, Andhra Pradesh 534101, India

⁴ Department of Mechanical Engineering, Sri Padmavathi Mahila Visvavidyalam, Tirupati, Andhra Pradesh 517502, India

⁵ Department of Electronics and Communication Engineering, Sagi Rama Krishnam Raju Engineering College, Bhimavaram, Andhra Pradesh 534202, India

an energy source to melt wire or powder materials. In the last two decades, AM has gained prominence due to its considerable advantages over traditional subtractive methods. It significantly reduces material waste, optimizes material properties, and shortens lead times for component applications [1]. While powder-based AM technologies are typically used for smaller parts, medium-to-large-scale components require a different approach. Wire arc additive manufacturing (WAAM) has recently emerged as a cost-effective alternative for producing medium-to-large-scale components. Offering several significant advantages, such as enhanced fabrication flexibility, better control, and easier automation, wire-based AM uses primarily three energy sources: electron and laser beams, along with plasma arc. However, beam-based methods, being more costly and complex, contrast with plasma arc processing, which is more economical due to lower hardware costs. Consequently, WAAM, particularly based on Gas Metal Arc welding (GMAW), has become a focus of this paper's research [3]. It is favored for its simplicity, stability, minimal maintenance needs, and the absence of costly tooling requirements.

Duplex ferritic–austenitic stainless steels (DSS) have a variety of uses due to their exceptional mix of good mechanical performance and superior corrosion resistance. Arc welding of flat and tubular components is the most prevalent DSS fabrication process. Nevertheless, casting is also used for the fabrication of complex shapes [4]. Additive manufacturing (AM) of DSS has recently been practiced using wire as feedstock material [5]. The microstructure of DSS is ferritic–austenitic. The optimal properties of these alloys are said to be achieved when the ferrite/austenite proportion is 50/50 [6]. A correct balance of ferrite/austenite is one of the most important criteria in manufacturing techniques such as welding, casting, and more recently, AM. The thermal cycle and chemical composition are the two main factors that affect phase fraction in DSS. The strongest austenite-forming elements in DSS, nickel and nitrogen, play a key role in the solid-state precipitation of austenite following a completely ferritic solidification [7]. To enhance austenite production, DSS uses high-nickel-content filler metals and/or nitrogen-containing shielding gases [8]. Slow cooling favors the formation of austenite but can also lead to the formation of harmful secondary phases such as carbides, nitrides (Cr_2N), and sigma (σ) [9]. On the other hand, rapid cooling prevents austenite formation and also precipitates non-equilibrium nitrides [10]. Therefore, precise selection of process parameters is crucial in order to fabricate a balanced DSS microstructure.

AM of duplex stainless steels has been studied in a few cases. Davidson et al. [11] used selective laser melting (SLM) to produce 2507 super-duplex stainless steel. The finished product contained 93 percent ferrite and a few Cr_2N particles. After a heat treatment at 1040 °C, the ferrite fraction decreased to 55%. Hengsbach et al. [12] employed SLM to manufacture a 2205 DSS component with a 99 percent ferrite fraction that was reduced to 66 percent after a 1000 °C heat treatment. Posch et al. [13] studied the WAAM of DSS using 2209 filler wire. With this method, they produced a part with an as-deposited ferrite number of 30 FN, displaying mechanical properties equivalent to those of the filler. Eriksson et al. [14] also utilized the WAAM technique to produce super-duplex stainless steel components, achieving a 20% ferrite content and good mechanical properties. Hosseini et al. [15] investigated the microstructural characteristics of DSS components deposited using the WAAM technique, achieving a 40% ferrite content, although sigma phases were observed at the grain boundaries.

Based on previous studies, WAAM has shown high potential for producing DSS with favorable microstructural and mechanical characteristics. It is also feasible to add additional DSS parts to the main component when enhanced mechanical properties are needed. However, the formation of microstructures and their influence on mechanical characteristics along the building direction of WAAM DSS cylindrical-shaped components remain unclear. The next possible step toward the WAAM of DSS cylindrical parts is to elucidate the relationship between microstructure and mechanical properties from region (1) to region (2) along the building direction. Therefore, the aim of this study is to investigate the mechanical properties (tensile strength, hardness, and impact toughness) and microstructural features of the bottom and top zones of WAAM 2209 DSS cylindrical parts that were made using the GMAW method

Materials and Methods

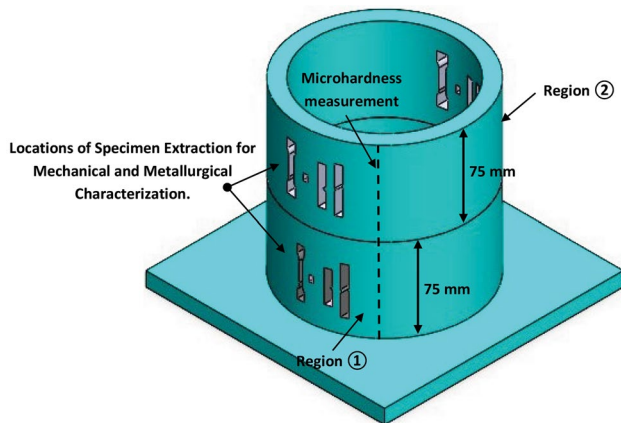
The WAAM setup used for this study consists of a three-axis automatic motion control system, a Fronius power source, welding torch, and a rotating table. The chemical composition of the 2209 DSS welding wire with diameter of 1.2 mm is given in Table 1. Gas metal arc welding additive manufacturing (GMAW-AM) was selected for its suitability in manufacturing duplex stainless steel cylindrical parts. It allows for precise control over heat input, essential for preserving the favorable microstructure and mechanical properties of

Table 1 Chemical elements of 2209 DSS filler wire

Specification	C	Si	Mn	P	S	Cr	Mo	Ni	Fe
AWS ER2209	0.014	0.29	1.29	0.018	0.001	22.47	3.1	8.37	Bal

Table 2 Optimized parameters of GMAW-AM process for fabricating 2209 DSS cylinder

Parameters	Value
Wire feed speed (m/min)	4.5
Current (Amp)	154
Voltage (V)	15.1
Welding speed (mm/min)	380
Pure argon (lit/min)	15

**Fig. 1** Schematic diagram, separation, and extraction of the WAAM 2209 DSS cylinder

duplex stainless steel. This technique offers high deposition efficiency and productivity, advantageous for constructing complex cylindrical geometries. Furthermore, GMAW-AM ensures a stable arc and consistent material deposition, crucial for achieving uniform layers and maintaining structural integrity in cylindrical components. In the GMAW process, there is a direct correlation between wire feed speed (WFS) and both current and voltage. The quality and geometry of the weld bead are crucial when using the WAAM technique to produce parts with cylindrical walls [22].

Numerous bead-on-plate trials were conducted by adjusting the WFS (ranging from 4 to 5.5 m/min) and welding speed (ranging from 320 to 430 mm/min) to identify the optimal parameters for fabricating cylindrical components with a wall thickness of 7–8 mm using the GMAW process. After several trials and adjustments, the appropriate parameters were successfully determined. These parameters were then utilized to fabricate a final cylindrical component with a height of 160 mm. Table 2 shows the deposition parameters. A single-layer multi-pass 2209 DSS cylindrical component was deposited on a mild steel substrate. The welding torch was positioned perpendicular to the substrate surface, which rotated with a mechanical motor during deposition. Figure 1 shows a schematic representation of the cylindrical component. The cylindrical component was divided into

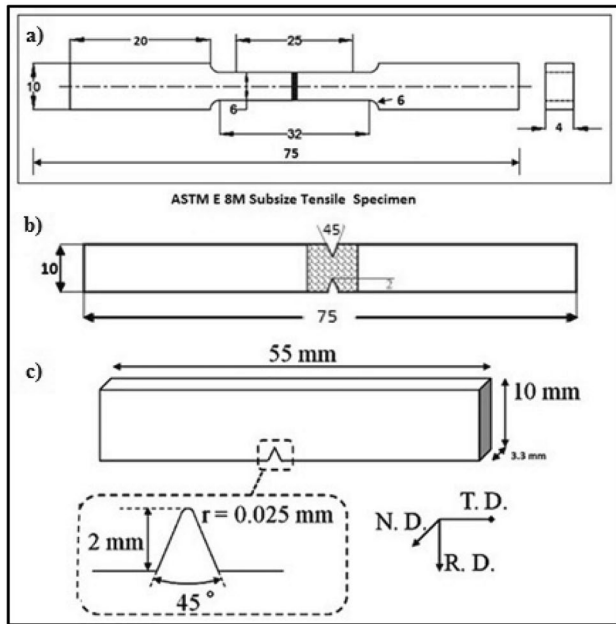
**Fig. 2** Photograph of the WAAM 2209 DSS straight cylindrical component**Fig. 3** Photograph of 2209 DSS cylindrical components (after machining)

two regions: the bottom area from the base plate to 75 mm (region (1)) and the middle area from 75 mm to 150 mm (region (2)), with specimen extraction details shown in Fig. 1. The manufactured 2209 DSS cylinder is displayed in Fig. 2.

After fabrication, the cylinder was divided into two sections using EDM cutting. The component was then machined to achieve a smooth surface finish and to minimize tool pressure using carefully selected machining parameters. The cutting speed was maintained between 100 and 180 mm/min, with a feed rate ranging from 0.1 to 0.4 mm/rev, and a depth of cut set between 0.2 and 0.6 mm. Appropriate lubrication was applied throughout the process to enhance the machining operation and ensure the integrity of the surface finish. The machining of the fabricated cylinder was performed to assess the quality of the deposits. Figure 3 displays a

Table 3 Geometry of the fabricated WAAM 2209 DSS cylinder

Geometry	Value
Wall width (mm)	7 ± 1
Single bead height (mm)	1.98 ± 1
Diameter of component (mm)	115 ± 1
Total component height (mm)	159 ± 1

**Fig. 4** Dimensions of specimens, (a) smooth tensile, (b) notch tensile, (c) Charpy impact toughness

photograph of the machined 2209 DSS cylinder, which has a wall thickness of 4 mm. Table 3 shows the geometry of the WAAM cylinder.

Specimens were vertically extracted from the cylindrical wall for microstructural examination, hardness, tensile, and impact testing [16]. Figure 4 shows the dimensions of the specimens. Tensile specimens were shaped according to the ASTM E8M standard and tested at room temperature on a servo-controlled mechanical testing machine (H50KL) with a cross-head speed of 0.5 mm/min. Charpy impact specimens were prepared following the ASTM A370 sub-size standard and tested using a pendulum-type impact testing machine (ASTM 1E-IT-30). Three smooth tensile, two notched tensile, and three impact specimens from regions (1) and (2) were tested, with the results averaged from three trials for analysis (as shown in Fig. 5). Scanning electron microscopy (SEM) was used to examine the fracture morphology of the tested impact and tensile specimens. Hardness was measured on the deposited wall using a Vickers hardness tester (load 0.5 kg, dwell time 10 s) at a position 1 mm from the surface in regions (1) and (2). The average hardness was calculated from eight measurements taken in each region. The microstructural examination was conducted on the mid-section of mirror-polished metallography samples, which were etched with 40 wt.% NaOH. The macrostructure of the produced component was studied using a stereozoom macroscope, and the etched microstructural samples were examined at various magnifications using an optical microscope (OM).

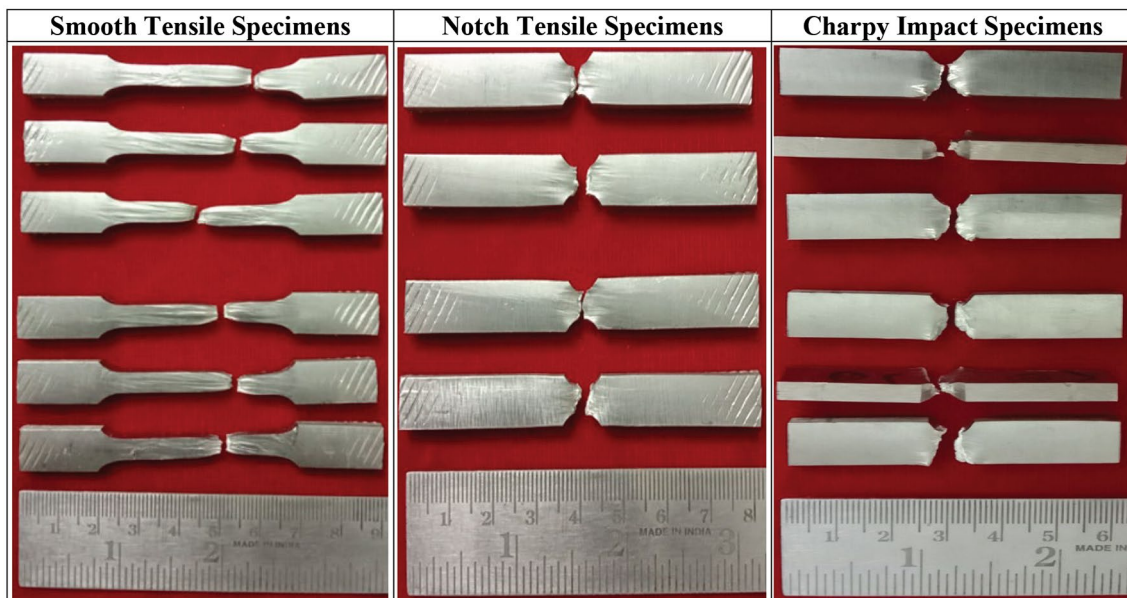
**Fig. 5** Photographs of the smooth tensile, notch tensile, and Charpy impact specimens (after testing)

Table 4 Mechanical properties of region (1) and region (2) of the 2209 DSS component

Sample	UTS, MPa	0.2% YS, MPa	Elongation in 25 mm gauge length, %	Notch tensile strength, MPa	Notch strength ratio, %	Impact toughness at RT, J
Region (1)	790	594	59.12	905	1.145	154
Region (2)	750	566	55.64	884	1.178	118

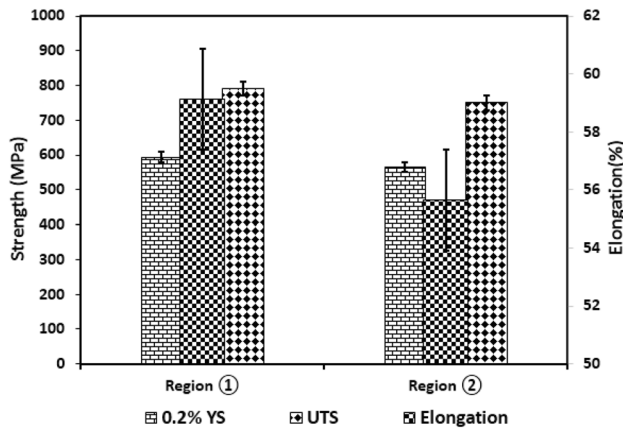


Fig. 6 Tensile properties of WAAM 2209 DSS cylinder

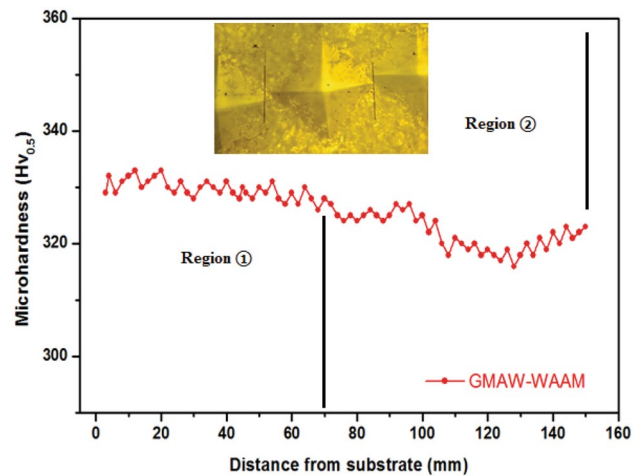


Fig. 7 Microhardness distribution of the WAAM 2209 DSS cylinder

Results and Discussion

Mechanical Properties

Table 4 presents the average tensile properties of the GMAW-AM 2209 DSS cylinder, and the comparison of these properties between regions (1) and (2) is illustrated in Fig. 6. In region (1), the average values of ultimate tensile strength (UTS), yield strength (YS), and elongation (EL) are 790 MPa, 594 MPa, and 59.12%, respectively. In contrast, in region (2), the UTS, YS, and EL are 750 MPa, 566 MPa, and 55.64%, respectively, indicating a decrease in tensile properties from region (1) to region (2). The specimens from region (1) exhibited higher UTS, YS, and EL compared to those from region (2).

Table 4 also shows the impact toughness values for regions (1) and (2) of the GMAW-AM 2209 DSS cylinder. Figure 5 includes photographs of the impact specimens after testing. The impact toughness (154 J) in region (1) was higher than in region (2). This reduction in toughness in region (2) is primarily attributed to decreased ductility, which is linked to variations in the microstructural morphology of the GMAW-WAAM cylinder.

Figure 7 displays the variation in microhardness along the building direction from region (1) to region (2), with a noticeable decrease in hardness toward region (2). The average microhardness values for regions (1) and (2) are

Table 5 Average microhardness of region (1) and region (2) of the 2209 DSS cylindrical component

Location	Average hardness, HV _{0.5}
Region (1)	329 ± 2
Region (2)	301 ± 1

listed in Table 5. This difference in microhardness is attributed to variations in phase composition and ferrite content across the two regions. These differences in mechanical properties are further discussed in the discussion chapter, focusing on the relationship with microstructural features and ferrite content.

Fractography

The fracture morphologies of the unnotched, notched, and impact toughness coupons of the manufactured cylinder are illustrated in Fig. 8 for different locations. Numerous dimples were observed on the fracture surfaces in regions (1) and (2), and the depth of the dimples decreased as the number of layers increased from region (1) to region (2). The size and depth of the dimples, which are directly related to ductility and strength, were greater in region (1) than in region (2) [17]. The tensile load increased the normal tensile stress leading to a rise in the number of voids. Consequently,

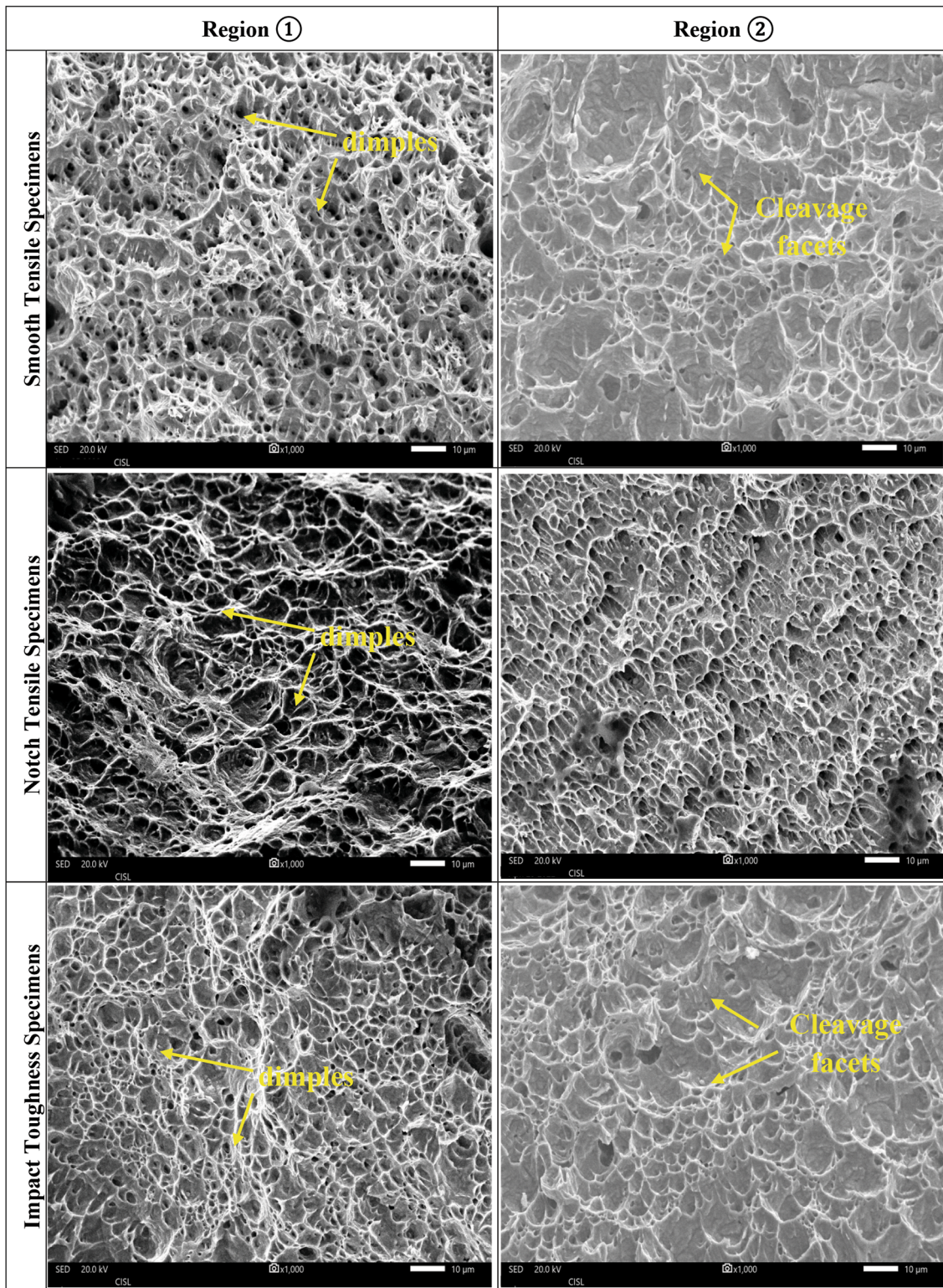


Fig. 8 SEM fractographs of the WAAM 2209 DSS component

the development and coalescence of these voids led to the fracture of the coupons. In region (1) of the cylinder, void coalescence with ductile fracture characteristics was the

primary type of fracture. However, in region (2), the number of dimples significantly decreased, and cleavage facets were observed, suggesting a transition to a mixed fracture

mechanism. This change from a predominantly ductile failure mode in region (1) to a mixed mode (ductile/brittle) in region (2) was influenced by the σ -phase [18]. This shift is one of the reasons for the observed reduction in elongation and ductility (toughness) in region (2) of the WAAM 2209 DSS cylinder.

Microstructure Analysis

The microstructures of region (1) of the WAAM 2209 DSS cylinder fabricated using the GMAW-AM process are displayed in Fig. 9. Figure 9a shows a schematic diagram from the bottom to the middle zone of the cylinder. The deposited

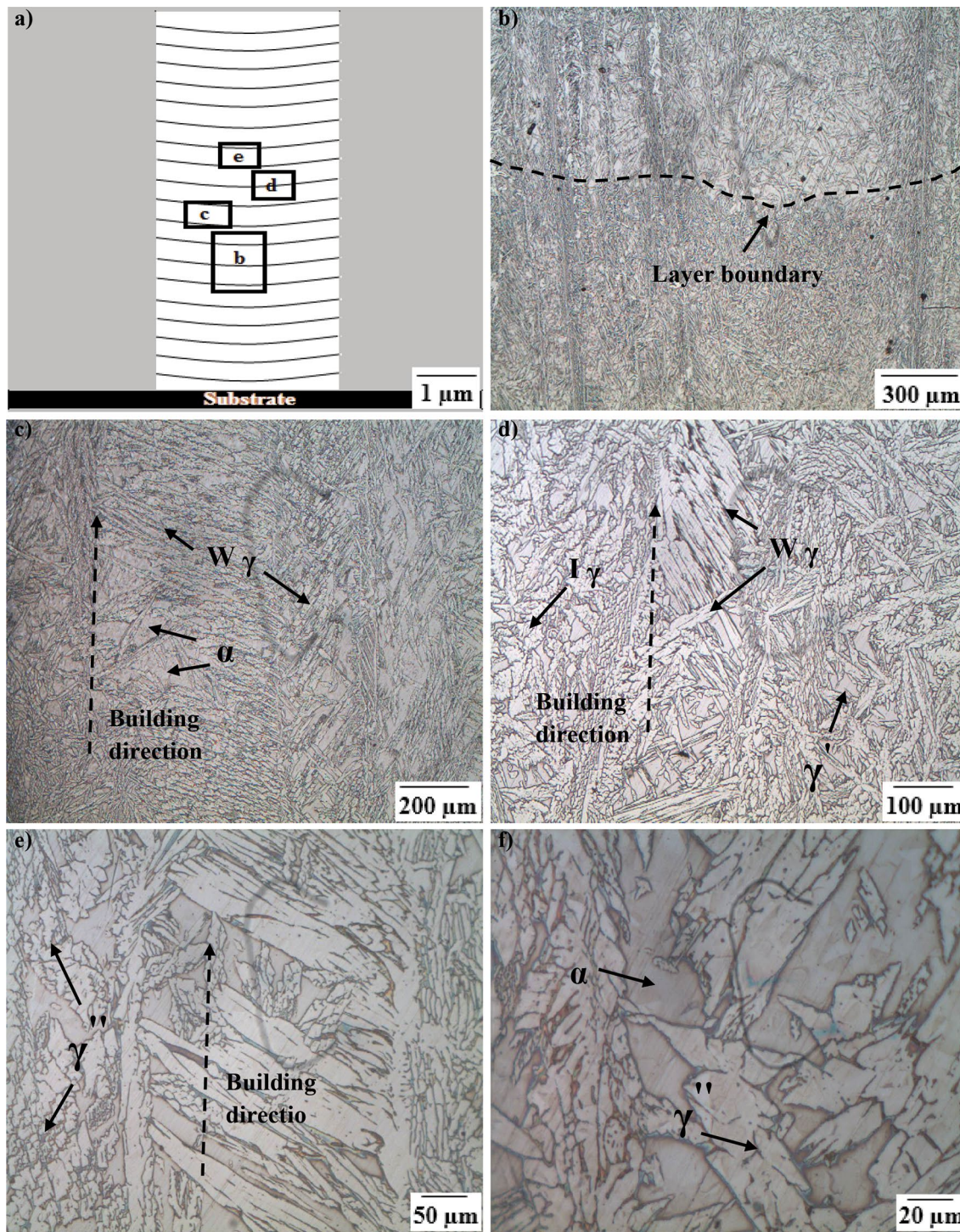


Fig. 9 Optical micrographs of region (1)

layers are completely welded, and the fusion lines are clearly visible in Fig. 9b, showing that the weld is free of major flaws. The WAAM 2209 DSS cylinder consists of various austenite morphologies within an α -ferrite matrix. As shown in Fig. 9c, the microstructure in region (1) was composed of Widmanstätten austenite and α -ferrite, with a higher amount of ferrite and finer Widmanstätten grains observed in Fig. 9e. This region cools rapidly due to its proximity to the substrate, resulting in fine features. According to Yang et al. [19], intragranular austenite and elongated Widmanstätten phases form during slow cooling at high temperatures. However, as illustrated in Fig. 9d, these morphologies are coarsened along the building direction. The newly formed layer remelts the previously deposited layer, leading to the formation of harder Widmanstätten austenite [20], instead of intragranular austenite. Figure 9d also shows secondary austenite morphologies in the direction of building, which form at lower temperatures in the transition zone between two layers from metastable ferrite [21]. As shown in Fig. 9e, γ grows in the ferrite grains along the building direction of the GMAW-AM cylinder, fostered by slow cooling within the temperature range of 500 to 800 °C. The ferrite content is higher in this region, as shown in Fig. 9e. Figure 9f displays the microstructure from Fig. 9e at a higher magnification. Due to the heat input and rapid cooling rate, this region reaches a high temperature, rising above the solution temperature. During cooling, austenite forms at the boundaries of ferrite grains, leading to an increase in ferrite content driven by significant ferritic grain development [22].

Figure 10 depicts the microstructure of region (2) of the 2209 DSS cylinder. Figure 10a shows the schematic diagram for the middle-to-top zone of the WAAM 2209 DSS cylinder. Figure 10b illustrates the austenite morphologies in region (2), which consist of various forms embedded within a ferrite matrix. Region (2) is characterized by four austenite morphologies: Widmanstätten austenite, intragranular austenite, secondary austenite, and grain boundary austenite. The ferrite phase was encircled by grain boundary austenite (GBA). A small amount of fine intragranular austenite (IGA) and small Widmanstätten austenite (WA) nucleated close to the GBA, which expanded along the building direction within the ferrite grains. The secondary austenite formed was finer than the primary austenite due to the multiple thermal cycles. The size of ferrite grains and the morphology of austenite changed from region (1) to region (2), with the WA and GBA morphologies becoming coarser. Similarly, the size of IGA varied significantly, while the ferrite grain size increased gradually, as shown in Fig. 10c and d. At slow cooling rates, different types of austenite morphologies with higher content occur in the GMAW-AM cylinder, as shown in Fig. 10d. Figure 10e shows the austenite morphologies at higher magnification in the ferrite matrix of the GMAW-AM cylinder at faster cooling rates.

EDS analysis was conducted using a SEM equipped with EDS to analyze the composition of the phases in region (2) of the WAAM 2209 DSS cylinder. Sigma phase (σ) was observed in the SEM images of the GMAW-AM cylinder, although it was not visible in the optical micrographs. The ferrite, austenite, and sigma phases are shown in the SEM image (Fig. 11c) of the GMAW-AM 2209 DSS cylinder. Figure 11d and e displays the EDS spectrum in region (2) of the WAAM 2209 DSS component. The chemical elements of each phase are listed in Table 6. Mo and Cr were primarily detected in the ferrite matrix, while Ni was mostly found in the austenite matrix. Thus, Mo and Cr promote ferrite formation, whereas Ni promotes austenite. According to EDS results, the produced sigma phase has a higher Cr content than the other two phases. The observed Cr/Mo ratio in the sigma phase was consistent with the value reported by Wang et al. [23] for sigma phases in chromium-based systems. The temperature during solidification greatly impacts the sigma phases in the GMAW-AM 2209 DSS cylinder, and controlling the main harmful sigma phase that forms at temperatures between 500 and 1100 °C is crucial during the GMAW-AM process to avoid degrading the toughness and ductility of the 2209 DSS cylinder. The distribution of sigma phase in region (2) was observed at the austenite boundaries, similar to that in traditional DSS. The σ -phase formed rapidly at the boundaries between the γ and ferrite phases due to the high interfacial energy.

Discussion

The microstructure of the GMAW-AM cylinder varies from region (1) to region (2) due to differences in heat flow and welding cooling rates between these areas. Figure 12 presents the Fe–Cr–Ni (pseudo-binary) ternary diagram [24]. According to this diagram, the ferrite-to-austenite phase transition in DSS occurs during the solidification process at temperatures ranging from 1200 to 800 °C (δ -solvus temperature) [25]. Slower cooling in region (2) results in higher austenite content because it allows more time for austenite nucleation. Additionally, the solid-state phase change from ferrite to austenite during solidification is another factor influencing the austenite proportion. The higher solidification temperature range of 1200–800 °C permits more time for this solid-state phase transition to occur. The duration of solidification gradually increases from region (1) to region (2), aiding in the transformation of ferrite into austenite [26]. Consequently, the ferrite content decreases from region (1) to region (2).

The microhardness measurements of the WAAM 2209 DSS cylinder are consistent with its microstructural characteristics. Hardness decreases from region (1) to region (2) but increases in the cylinder's final layers, which is consistent with recently reported data [27]. The average

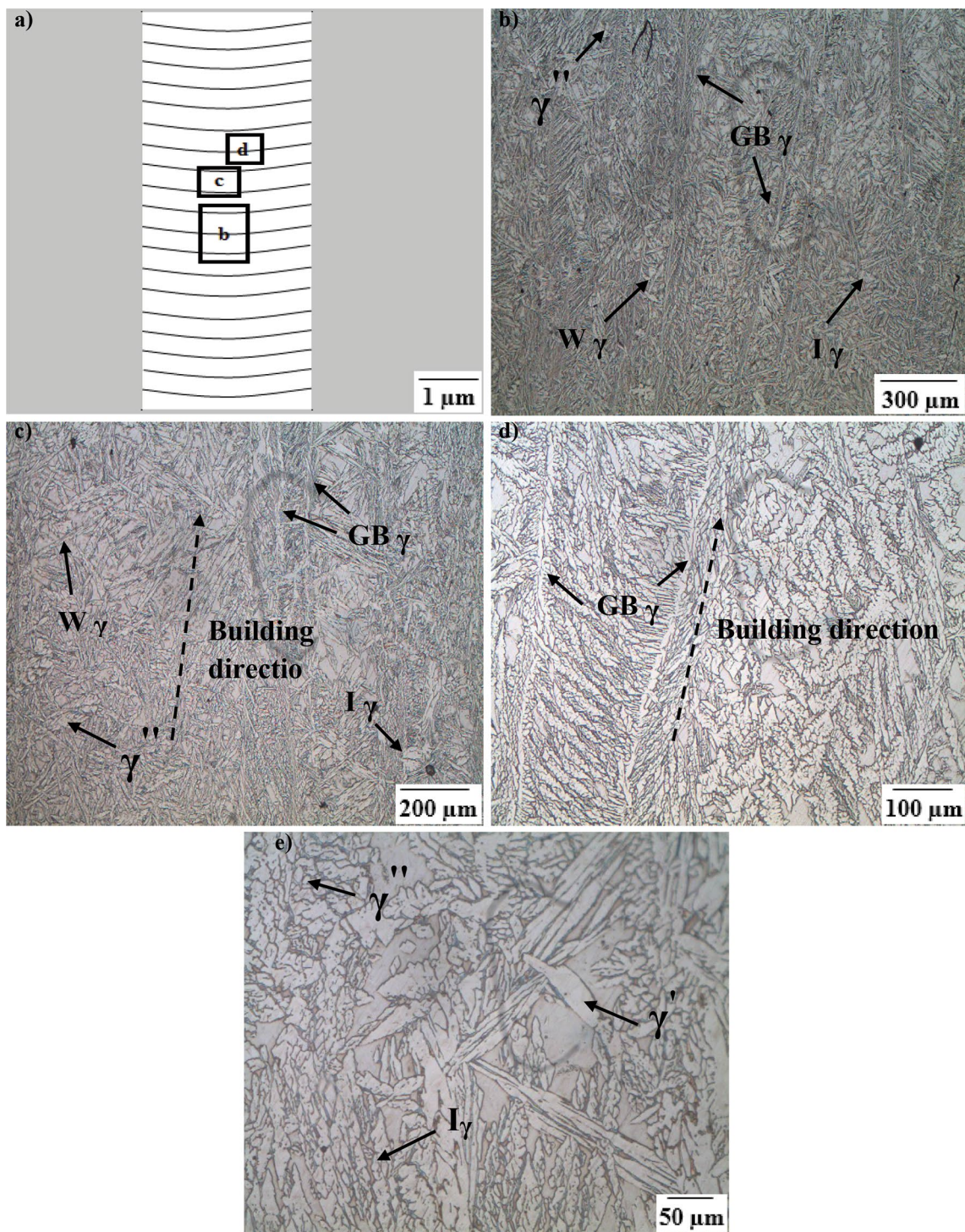


Fig. 10 Optical micrographs of region (2)

microhardness values for the GMAW-AM cylinder range from 301 to 327 $HV_{0.5}$. Region (1), which has a higher ferrite content, exhibits an average hardness of 327 $HV_{0.5}$. In contrast, region (2), with reduced ferrite content, shows an average hardness of 293 $HV_{0.5}$. There is a notable difference

in mechanical properties from region (1) to region (2). Similar differences are reported in WAAM-fabricated DSS parts [28, 29]. These differences in UTS and hardness between regions are primarily due to variations in microstructural features and grain size. The UTS and hardness in region

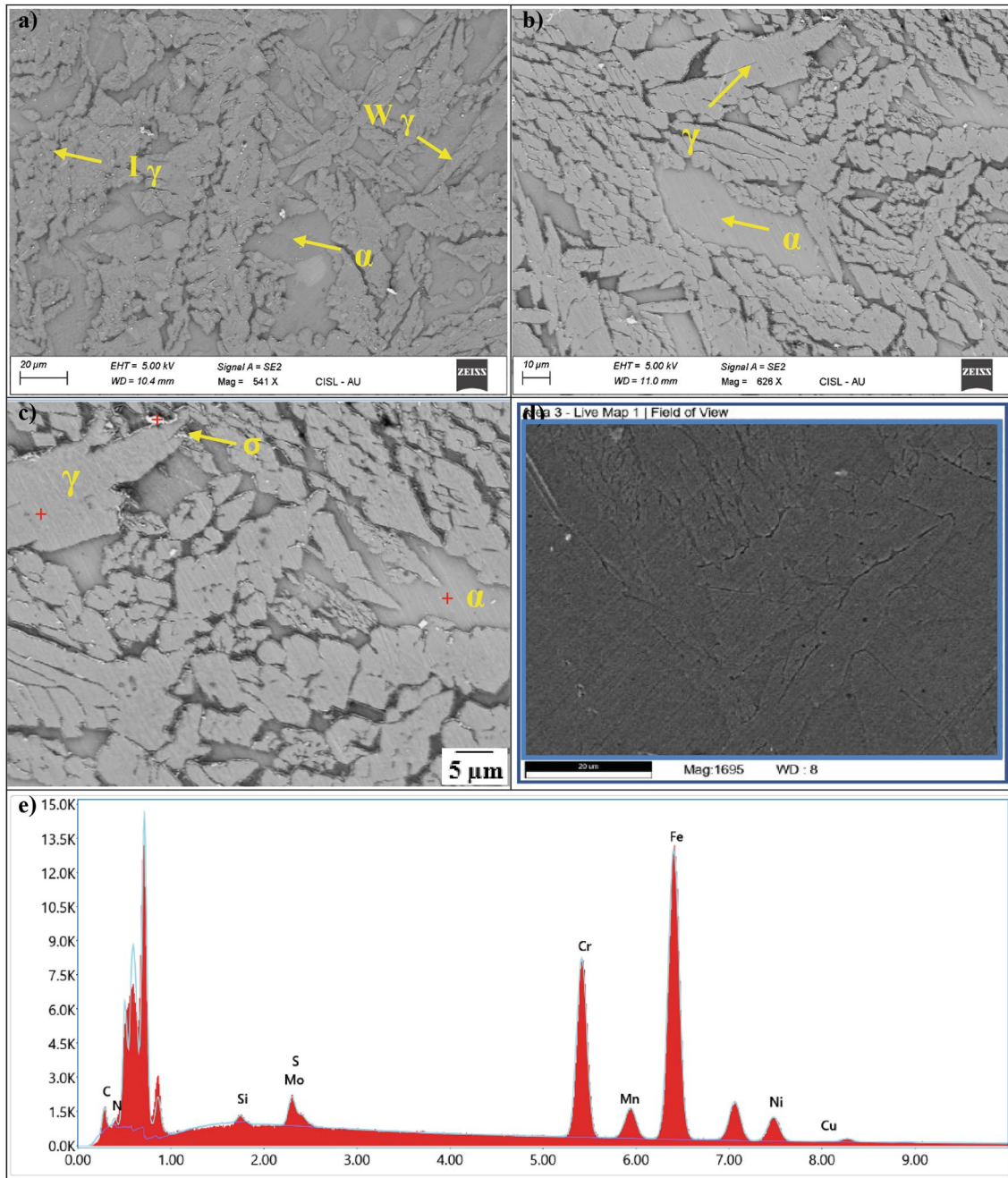


Fig. 11 (a–c) SEM micrographs of region (2) (d–e) EDS spectrum of region (2)

Table 6 Chemical elements of each phase in the GMAW-AM 2209 DSS cylinder (wt.%)

Phase	Mn	Si	Ni	Cr	Mo
Ferrite	1.72	0.51	6.01	25.21	3.45
Austenite	2.12	0.44	9.76	21.98	3.21
σ (Cr/Mo)	1.01	0.64	4.12	31.45	5.98

(1) are higher than in region (2) because it contains more ferrite, primary and secondary austenite, intragranular austenite, and Widmanstätten austenite.

In the GMAW-AM cylinder, hardness decreased from region (1) to region (2) due to variations in grain size, microstructural features, and ferrite content. From region (1) to region (2), the grain size increased, while the ferrite content decreased. The primary reasons for the increase in grain size and decrease in ferrite content are the slow

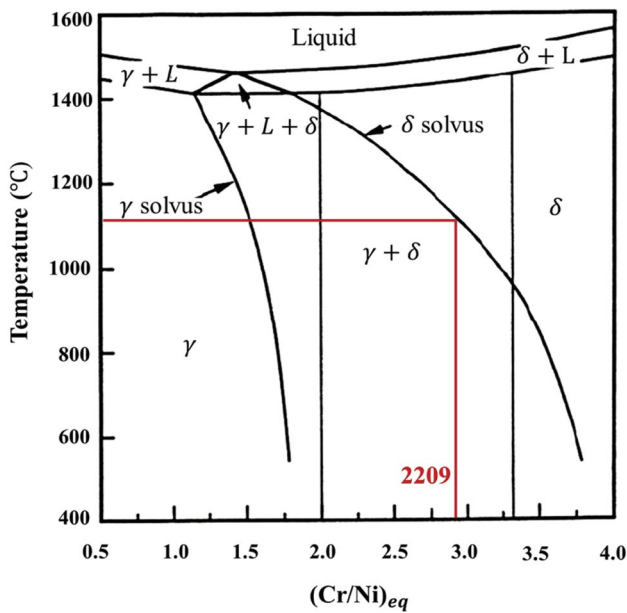


Fig. 12 Pseudo-binary Fe–Cr–Ni diagram

cooling rates characteristic of the GMAW-AM process. Coupons tested from region (2) exhibited lower ductility and toughness compared to those from region (1), largely due to the formation of harmful sigma phases resulting from the slow cooling rate. According to Zhang et al. [30], detrimental intermetallic phases such as λ and σ are responsible for the decrease in impact toughness and elongation in specimens deposited in the WAAM 2594 DSS components. The tensile properties of the current investigation along with those of wrought 2209 DSS alloy and 2209 DSS filler wire are listed in Table 7 [30, 31]. Compared to the wrought 2209 DSS alloy and the 2209 DSS filler wire, the coupons tested from regions (1) and (2) of the WAAM 2209 DSS parts in the current research demonstrated equal or better tensile properties. This is mainly attributed to the favorable microstructural features of the WAAM 2209 DSS parts.

Conclusions

The 2209 DSS cylindrical component was successfully fabricated using the GMAW-AM technique. The mechanical and microstructural characteristics were studied across different regions of the cylinder. The following conclusions can be drawn from this study:

- (i) The tensile properties of the GMAW-AM 2209 DSS cylinder decreased from region (1) to region (2). Specimens from region (1) exhibited higher UTS, YS, and EL compared to those from region (2).
- (ii) Impact toughness in region (2) was lower than that in region (1). The specimens tested from region (1) demonstrated an impact toughness of 154 J, which was significantly higher than that of the specimens from region (2). The presence of the detrimental intermetallic σ -phase is the main reason for the decreased impact toughness and elongation in region (2) of the WAAM 2209 DSS component.
- (iii) Hardness decreased from region (1) to region (2), with higher values observed in region (1) and a reduction along the building direction to region (2). Variations in microhardness were caused by differences in phases and ferrite content between regions (1) and (2). The production of a greater ferrite content, along with primary and secondary austenite, intragranular austenite, and Widmanstätten austenite, resulted in higher UTS and hardness in region (1) compared to region (2).
- (iv) The primary phase balance in the manufactured cylinder was significantly influenced by complex heat cycles and the cooling rate during the WAAM process. A longer solid-state phase transition time and a lower cooling rate led to a higher austenite percentage from region (1) to region (2).

Table 7 Comparison of tensile properties of GMAW-AM 2209 DSS cylinder with widely used wrought 2205 DSS alloy, ER2205 DSS annealed condition, and ER2209 DSS filler wire

Process	Specimen location	YS (MPa)	UTS (MPa)	EL (%)	References	
Wrought 2205 DSS	...	590	779	...	[27]	
	...	590	786	48	[28]	
ER2209 DSS filler wire	...	560	720	...	[30]	
ER2205 DSS annealed condition	620	25	[31]	
Present study	GMAW-WAAM 2209 DSS cylinder	Region (1)	594	790	59.12	...
		Region (2)	566	750	55.64	

Acknowledgments The authors are grateful for the financial assistance and comprehensive infrastructure support provided by SRM University-AP, Mangalagiri, India. Additionally, the first author would like to acknowledge the Centre for Materials Joining & Research (CEMAJOR) at the Department of Manufacturing Engineering, Annamalai University, Annamalai Nagar, India, for their technical support.

References

- B. Prasanna Nagasai, S. Malarvizhi, V. Balasubramanian, Mechanical properties of wire arc additive manufactured carbon steel cylindrical component made by cold metal transfer arc welding process. *Materi. Test.* **64**, 260–271 (2022). <https://doi.org/10.1515/mt-2021-2051>
- B. Prasanna Nagasai, S. Malarvizhi, V. Balasubramanian, Characterisation of a wire arc additive manufactured 308L stainless steel cylindrical component. *Materi. Test.* **64**, 1–11 (2022). <https://doi.org/10.1515/mt-2022-0171>
- B. Prasanna Nagasai, S. Malarvizhi, V. Balasubramanian, Mechanical properties and microstructural characteristics of Al–Mg alloy cylindrical component manufactured by wire arc additive manufacturing process. *Metallogr. Microstruct. Anal.* **11**, 199–211 (2022). <https://doi.org/10.1007/s13632-022-00841-2>
- J.C. Lippold, D.J. Kotecki, *Welding Metallurgy and Weldability of Stainless Steels* (Wiley-Interscience, Hoboken, NJ, USA, 2005)
- L. Karlsson, Welding of duplex stainless steels—a review of current recommendations. *Weld. World.* **56**, 65–76 (2012). <https://doi.org/10.1007/BF03321351>
- L. Mraz, F. Matsuda, Y. Kikuchi, Temper embrittlement of cast duplex stainless steels after long-term aging. *Trans. JWRI.* **23**, 213–222 (1994)
- B. Wu, Z. Pan, D. Ding, A review of the wire arc additive manufacturing of metals: properties, defects and quality improvement. *J. Manuf. Process.* **35**, 127–139 (2018)
- M. Martins, L.C. Casteletti, Sigma phase morphologies in cast and aged super duplex stainless steel. *Mater. Charact.* **60**, 792–795 (2009). <https://doi.org/10.1016/j.jmapro.2018.08.001>
- B. Messer, V. Oprea, A. Wright, Duplex stainless steel welding: best practices. *Stainless Steel. Weld. World.* **22**, 53–63 (2007)
- A.V. Hosseini, L. Karlsson, T. Engelberg, Time temperature-m precipitation and property diagrams for super duplex stainless steel weld metals. *Weld. World.* **62**, 517–533 (2018). <https://doi.org/10.1007/s40194-018-0548-z>
- K. Davidson, S. Singamneni, Selective laser melting of duplex stainless steel powders: an investigation. *Mater. Manuf. Process.* **31**, 1543–1555 (2016). <https://doi.org/10.1080/10426914.2015.1090605>
- F. Hengsbach, P. Koppa, K. Duschik, Duplex stainless steel fabricated by selective laser melting—microstructural and mechanical properties. *Mater. Des.* **133**, 136–142 (2017). <https://doi.org/10.1016/j.matdes.2017.07.046>
- G. Posch, K. Chladil, H. Chladil, Material properties of CMT—metal additive manufactured duplex stainless steel blade-like geometries. *Weld. World.* **61**, 873–882 (2017). <https://doi.org/10.1007/s40194-017-0474-5>
- M. Eriksson, M. Lervåg, C. Sørensen, Additive manufacture of superduplex stainless steel using WAAM. *MATEC Web Conf. EDP. Sci.* **188**, 1–8 (2018). <https://doi.org/10.1051/mateconf/201818803014>
- A.V. Hosseini, M. Högström, K. Hurtig, Wire-arc additive manufacturing of a duplex stainless steel: thermal cycle analysis and microstructure characterization. *Weld. World.* **63**, 975–987 (2019). <https://doi.org/10.1007/s40194-019-00735-y>
- B. Prasanna Nagasai, S. Malarvizhi, V. Balasubramanian, Characterisation of Al–Mg alloy cylindrical component made by wire arc additive manufacturing using cold metal transfer arc welding process. *Trans. Indian Inst. Met.* **75**, 2019–2030 (2022). <https://doi.org/10.1007/s12666-022-02583-9>
- B. Prasanna Nagasai, S. Malarvizhi, V. Balasubramanian, A study on wire arc additive manufacturing of 308L austenitic stainless steel cylindrical component: optimization, microstructure and mechanical properties. *Proc. Inst. Mech. Eng. Part B: J Eng. Manuf.* **236**, 1–13 (2022). <https://doi.org/10.1177/09544054221129471>
- F. Binesh, A. Bahrami, M. Hebel, Preservation of natural phase balance in multi-pass and wire arc additive manufacturing-made duplex stainless steel structures. *J. Mater. Eng. Perform.* **30**, 2552–2565 (2021). <https://doi.org/10.1007/s11665-021-05593-8>
- L. Yang, W. Lu, Z. Liu, Location-dependent microstructure and properties for plasma arc additively manufactured duplex stainless steel ER2209 wire. *J. Mater. Eng. Perform.* **30**, 6788–6800 (2021). <https://doi.org/10.1007/s11665-021-06005-7>
- A.J. Ramirez, J.C. Lippold, S.D. Brandi, The relationship between chromium nitride and secondary austenite precipitation in duplex stainless steels. *Metall. Mater. Trans. A.* **34**, 1575–1597 (2003). <https://doi.org/10.1007/s11661-003-0304-9>
- Y. Zhang, F. Cheng, S. Wu, Improvement of pitting corrosion resistance of wire arc additive manufactured duplex stainless steel through POST-manufacturing heat-treatment. *Mater. Charact.* **171**, 1–11 (2021). <https://doi.org/10.1016/j.matchar.2020.110743>
- W. Liu, X. Lu, P. Boulet, Influence of atomic order on the enthalpy of formation and bulk modulus of the sigma phase. *Fluid. Phase. Equilib.* **459**, 238–243 (2018). <https://doi.org/10.1016/j.fluid.2017.10.006>
- Y. Wang, J. Han, H. Wu, Effect of sigma phase precipitation on the mechanical and wear properties of Z3CN200.9M cast duplex stainless steel. *Nucl. Eng. Des.* **259**, 1–7 (2013)
- F. Mirakhorli, F. Malek Ghaini, M.J. Torkamany, Development of weld metal microstructures in pulsed laser welding of duplex stainless steel. *J. Mater. Eng. Perform.* **21**, 2173–2176 (2012). <https://doi.org/10.1007/s11665-012-0141-3>
- J. Verma, R.V. Taiwade, Effect of welding processes and conditions on the microstructure, mechanical properties and corrosion resistance of duplex stainless steel weldments—a review. *J. Manuf. Process.* **25**, 134–152 (2017). <https://doi.org/10.1016/j.jmapro.2016.11.003>
- C.R. Xavier, H.G.D. Junior, J.A.D. Castro, An experimental and numerical approach for the welding effects on the duplex stainless steel microstructure. *Mat. Res.* **18**, 489–502 (2015). <https://doi.org/10.1590/1516-1439.302014>
- E. Taban, E. Kaluc, Welding behaviour of duplex and superduplex stainless steels using laser and plasma arc welding processes. *Weld. World.* **55**, 48–57 (2011). <https://doi.org/10.1007/BF03321307>
- H. Fatemeh, B. Farrokh, H. Mark, Thermal modeling and characterization of wire arc additive manufactured duplex stainless steel. *J. Mater. Proc. Tech.* **272**, 58–71 (2019). <https://doi.org/10.1016/j.jmatprotec.2019.05.003>
- H. Fatemeh, B. Farrokh, H. Mark, Preservation of natural phase balance in multi-pass and wire arc additive manufacturing-made duplex stainless steel structures. *J. Mater. Eng. Per.* **30**, 2552–2565 (2021). <https://doi.org/10.1007/s11665-021-05593-8>
- X. Zhang, K. Wang, Q. Zhou, Microstructure and mechanical properties of TOP-TIG-wire and arc additive manufactured super duplex stainless steel (ER2594). *Mater. Sci. Eng. A.* **762**, 1–12 (2019). <https://doi.org/10.1016/j.msea.2019.138097>
- A.V. Jebaraj, L. Ajaykumar, C.R. Deepak, Weldability, machinability and surfacing of commercial duplex stainless

steel aisi2205 for marine applications—a recent review. *J. Adv. Res.* **8**, 183–199 (2017). <https://doi.org/10.1016/j.jare.2017.01.002>

Publisher's Note Springer Nature remains neutral with regard to jurisdictional claims in published maps and institutional affiliations.

Springer Nature or its licensor (e.g. a society or other partner) holds exclusive rights to this article under a publishing agreement with the author(s) or other rightsholder(s); author self-archiving of the accepted manuscript version of this article is solely governed by the terms of such publishing agreement and applicable law.